

REPORT DOCUMENT		0543	
Public reporting burden for this collection of information is estimated at 1 hour per response, including the time for reviewing instructions, gathering and maintaining the data needed, and completing and maintaining the collection of information, including suggestions for reducing this burden. Send comments regarding this burden estimate or any other aspect of this collection of information, including suggestions for reducing this burden, to Washington Operations and Reports, 1315 Jefferson Davis Highway, Suite 1204, Arlington, VA 22202-4307, and to the Office of Management and Budget, Paperwork Reduction Project (0704-0188), Washington, DC 20503.			
1. AGENCY USE ONLY (Leave blank)		2. REPORT DATE	3. REPORT TYPE AND DATES COVERED
		15 Jul 97	Final 01 Mar 93 to 28 Feb 97
4. TITLE AND SUBTITLE		5. FUNDING NUMBERS	
MBE Growth and Characterization of Zinc Blende GAN and GAN/AlN Structures		61102F 2305/ES	
6. AUTHOR(S)		7. PERFORMING ORGANIZATION NAME(S) AND ADDRESS(ES)	
Professor Song		Oklahoma State University 210 Life Sciences East Stillwater OK 74078-0266	
8. SPONSORING/MONITORING AGENCY NAME(S) AND ADDRESS(ES)		9. PERFORMING ORGANIZATION REPORT NUMBER	
AFOSR/NE 110 Duncan Aven RmB115 Bolling AFB DC 20332-8050		F49620-93-1-0211	
11. SUPPLEMENTARY NOTES			
12a. DISTRIBUTION/AVAILABILITY STATEMENT		12b. DISTRIBUTION CODE	
APPROVAL FOR PUBLIC RELEASED: DISTRIBUTION UNLIMITED			
13. ABSTRACT (Maximum 200 words)			
<p>This Program includes fundamental studies of Molecular beam epitaxial (MBE) growth of GaN and its related alloys and heterostructures. In addition, the optical and electrical properties of resultant materials were measured using a variety of spectroscopic techniques. The optical properties concentrated on optically-pumped stimulated emission and laser action in GaN/AlGaN heterostructures. The objective was to better understand the underlying physics of MBE growth, and the optical and electrical properties for GaN-based device application.</p>			
14. SUBJECT TERMS		15. NUMBER OF PAGES	
16. PRICE CODE		17. SECURITY CLASSIFICATION OF REPORT	
UCNCLASSIFIED		18. SECURITY CLASSIFICATION OF THIS PAGE	
UNCLASISIED		19. SECURITY CLASSIFICATION OF ABSTRACT	
UNCLASISIED		20. LIMITATION OF ABSTRACT	
III.			
Standard Form 298 (Rev. 2-89) <small>Prescribed by ANSI Std. Z39-18</small>			

NSN 7540-01-280-5500

Standard Form 298 (Rev. 2-89)
Prescribed by ANSI Std. Z39-18

AFOSR FINAL REPORT

PROGRAM DIRECTOR: **Dr. Mike Prairie**

PROJECT TITLE: **MBE Growth and Characterization
of Zincblende GaN and GaN/AlN
Structures**

CONTRACT NO: **AFOSR #F49620-93-1-0211**

PRINCIPAL INVESTIGATOR: **Dr. J.J. Song
Center for Laser & Photonics
Research & Dept. of Physics
Oklahoma State University
Stillwater, OK 74078
405-744-6575**

CO-PRINCIPAL INVESTIGATOR: **Dr. R.J. Hauenstein
Dept. of Physics
Oklahoma State University
Stillwater, OK 74078
405-744-5812**

REPORTING PERIOD: **3/1/93-4/30/97**

REPORTING DATE: **7/15/97**

MBE Growth and Characterization of Zinc-Blende GaN/AlN Structures

I. Introduction/Objectives

This program was a collaborative effort between Professors J. J. Song and R. J. Hauenstein at Oklahoma State University, which included fundamental studies of the molecular beam epitaxial (MBE) growth of GaN and its related alloys and heterostructures, as well as the optical and electrical properties of resultant materials using a variety of spectroscopic techniques. The objective was to better understand the underlying physics of MBE growth, the optical and electrical properties for GaN-based device application.

II. Publications

"Optical Properties and Lasing in GaN", in Physics and Applications of Group III Nitrides Semiconductor Compounds", J. J. Song and W. Shan; B. Gil, Ed. (Oxford University Press, London) 1997 (in press).

"Study of Surface-Emitted Stimulated Emission in GaN", S. Bidnyk, T.J. Schmidt, G.H. Park, and J.J. Song, Appl. Phys. Lett. (accepted for publication, August 1997).

"Femtosecond four-wave-mixing studies of nearly homogeneously broadened excitons of GaN", A.J. Fischer, W. Shan, G.H. Park, J.J. Song, D.S. Kim, D.S. Yee, R. Horning, and B. Goldenberg, Phys. Rev. B **56**, 1 (1997).

"Correlation of Biaxial Strains, Bound Exciton Energies, and Defect Microstructures in GaN Films Grown on AlN/6H-SiC (0001) Substrates", W.G. Perry, T. Zheleva, M.D. Bremser, R.F. Davis, W. Shan, and J.J. Song, J. Electr. Mats. **26**, 224 (1997).

"Linear and Nonlinear Optical Investigations of GaN and AlGaN/GaN Heterostructures", J.J. Song, A.J. Fischer, W. Shan, B. Goldenberg, and G.E. Bulman, Inst. Phys. Conf. Ser. **155**, 355 (1997).

"Binding Energy for the Intrinsic Excitons in Wurtzite GaN", W. Shan, B.D. Little, A.J. Fischer, J.J. Song, B. Goldenberg, W.G. Perry, M.D. Bremser, and R.F. Davis, Phys. Rev. B **54**, 16369, (1996).

"Optical Transitions in $\text{In}_x\text{Ga}_{1-x}\text{N}$ Alloys Grown by Metalorganic Chemical Vapor Deposition", W. Shan, B. Little, J.J. Song, Z.C. Feng, M. Schurman, and R.A. Stall, Appl. Phys. Lett. **69**, 3315 (1996).

"Optical Studies of GaN and GaN/AlGaN Heterostructures on SiC Substrates," W. Shan, A. J. Fischer, J. J. Song, G. E. Bulman, H. S. Hong, M. T. Leonard, W. G. Perry, M. D. Bremser, and R. f. Davis, *Appl. Phys. Lett.* **69**, 740 (1996).

"Optical Properties of Mg-GaN, GaN/AlGaN SCH Structures, and GaN on ZnO Substrates", H. Morkoc, W. Kim, O. Aktas, A. Salvador, D.C. Reynolds, M. Smith, G.D. Chen, J.Y. Lin, H.X. Jiang, T.J. Schmidt, X.H. Yang, W. Shan, J.J. Song, B. Goldenberg, C.W. Litton, and K. Evens, *Mat. Res. Soc. Symp. Proc.* **395**, 527 (1996).

"Growth of GaN by Gas-Source Molecular Beam Epitaxy by Ammonia and by Plasma Generated Nitrogen Radicals", W.S. Wong, N.Y. Li, H.K. Dong, F. Deng, S.S. Lau, C.W. Tu, J. Hays, S. Bidnyk, and J.J. Song, *J. of Crystal Growth* **164**, 159 (1996).

"Molecular Beam Epitaxial Growth of Eu-doped CaF₂ and BaF₂ on Si", X.M. Fang, T. Chatterjee, P.J. McCann, W.K. Liu, M.B. Santos, W. Shan, and J.J. Song, *J. Vac. Sci. Technol. B* **14**, 2267 (1996).

"Optical Studies of Epitaxial GaN Based Materials," J. J. Song, W. Shan, T. J. Schmidt, X. H. Yang, A. J. Fischer, S. J. Hwang, and B. Taheri, *SPIE Proc.*, **2693**, 86 (1996).

"Recent Progress in Optical Studies of Wide-Gap Nitrides for Optoelectronic Device Applications," W. Shan, T. J. Schmidt, X. H. Yang, J. J. Song, and B. Goldenberg, *Inst. Phys. Conf. Ser. No. 145*, 1151 (1996).

"Picosecond Four-Wave Mixing in GaN Epilayers at 532 nm," B. Taheri, J. Hays, J. J. Song, and B. Goldenberg, *Appl. Phys. Lett.* **68**, 587 (1996).

"Room-Temperature Stimulated Emission in GaN/AlGaN Separate Confinement Heterostructures Grown by Molecular Beam Epitaxy," T. J. Schmidt, X. H. Yang, W. Shan, and J. J. Song, *Appl. Phys. Lett.* **68**, 1820 (1996).

"Intensity Scan Determination of Two Photon Absorption and Nonlinear Refraction of C₆₀ in Toulene", B. Taheri, D. Appling, B. Jassemnejad, R. Powell, and J.J. Song, *Appl. Phys. Lett.* **68**, 1317 (1996).

"Spectroscopic Studies of GaN Grown by Metalorganic Chemical Vapor Deposition", W. Shan, J.J. Song, T.J. Schmidt, X.H. Yang, and B. Goldenberg, to be published in *International Journal of Solid State Electronics (TWN'95 Proceedings)* (1996).

"Time-resolved Exciton Luminescence in GaN Grown by Metalorganic Chemical Vapor Deposition", W. Shan, X.C. Xie, J.J. Song, and B. Goldenberg, *Appl. Phys. Lett.* **67**, 2512 (1996).

"Optical Properties of Wurtzite GaN Grown by Low-Pressure Metalorganic Chemical-Vapor Deposition", W. Shan, T. Schmidt, X.H. Yang, J.J. Song, and B. Goldenberg, *J. Appl. Phys.* **79**, 3691 (1996).

"Recent Progress in Optical Studies of Wurtzite GaN Grown by Metalorganic Chemical Vapor Depositon", W. Shan, T. Schmidt, X.H. Yang, J.J. Song, and B. Goldenberg, *Inst. Phys. Conf. Ser.* **145**, 1151.

"Strain Effects on Excitonic Transitions in GaN: Deformation Potentials," W. Shan, R. J. Hauenstein, A. J. Fischer, J. J. Song, W. G. Perry, M. D. Bremser, R. F. Davis, and B. Goldenberg, *Phys. Rev. B* **54**, 13460 (1996).

"Going Beyond the Mean-Filed Approximations of Alloys and Alloy Superlattices: A Few Puzzles Solved?" D.S. Kim, H.S. Ko, Y.S. Lim, Y.M. Kim, J.S. Lee, S.J. Rhee, W.S. Kim, S.C. Hong, Y.H. Yee, J.S. Khim, J.M. Jung, S. Huhr, J.H. Lee, J.S. Chang, B.D. Choe, J.C. Woo, P.H. Song, H.J. Choi, S.H. Jhi, J. Ihm, E.J. Shin, D. Kim, D.H. Woo, K.N. Kang, J.J. Song, *J. Opt. Soc. Am. B* **13**, 1210 (1996).

"Spatial and Dynamical Properties of Optical Phonons in $\text{Al}_x\text{Ga}_{1-x}\text{As}$ and $\text{GaAs}/\text{Al}_x\text{Ga}_{1-x}\text{As}$ Supperlattices: Beyond the Mean Field Approach", D.S. Kim, P.H. Song, S.H. Jhi, Y.S. Lim, E.J. Shin, Y.H. Yee, J.S. Khim, J. Ihm, J.H. Lee, J.S. Chang, D.H. Woo, K.N. Kang, D. Kim, J.J. Song, *Physica B* **219**, 684 (1996).

"Dynamics of Photoexcited Carriers in GaN", J.J. Song, W. Shan, B. Goldenberg, G.E. Bulman, and J.A. Edmond, to be published in *International Journal of Solid State Electronics (TWN'95 Proceedings)* (1996).

"Microscopic Processes during Electron Cyclotron Resonance Microwave Nitrogen Plasma-Assisted Molecular Beam Epitaxial Growth of Gan/GaAs Heterostructures: Experiments and Kinetic Modeling," Z. Z. Bandic, R. J. Hauenstein, M. L. O'Steen, and T. C. McGill, *J. Vac. Sci. Technol. A*, **14**, 2948 (1996).

"Atomic-Scale Structure and Electronic Properties of GaN/GaAs Superlattices", R. S. Goldman, B. G. Briner, R. M. Feenstra, M. L. O'Steen, and R. F. Hauenstein, *Appl. Phys. Lett.*, **69**, 3698 (1996).

"Kinetic Modeling of Microscopic Processes during Electron Cyclotron Resonance Microwave Plasma-Assisted Molecular Beam Epitaxial Growth of GaN/GaAs Heterostructures," Z. Z. Bandic, R. J. Hauenstein, M. L. O'Steen, and T. C. McGill, *Appl. Phys. Lett.* **68**, 1510 (1996).

"Reflection High Energy Electron Diffraction Study of Nitrogen Plasma Interactions with a GaAs (100) Surface," R. J. Hauenstein, D. A. Collins, X. P. Cai, M. L. O'Steen, and T. C. McGill, *Appl. Phys. Lett.* **66**, 2861 (1995).

"Schottky-Based Band Lineups for Refractory Semiconductors," M. W. Wang, J. O. McCaldin, J. F. Swenberg, T. C. McGill, and R. J. Hauenstein, *Appl. Phys. Lett.* **66**, 1974 (1995).

"Anion Exchange Reactions and Initial GaN Epitaxial Layer Formation under Nitrogen Plasma Exposure of a GaAs Surface," R. J. Hauenstein, D. A. Collins, M. L. O'Steen, Z. Bandic, S. J. Hwang, and T. C. McGill, *Mater. Res. Soc. Symp. Proc.* **388**, 259 (1995).

"Temperature Dependence of Interband Transitions in GaN Grown by Metalorganic Chemical Vapor Deposition", W. Shan, T.J. Schmidt, X.H. Yang, S.A. Hwang, J.J. Song and B. Goldenberg, *Appl. Phys. Lett.* **66**, 985, (1995).

"Above Room Temperature Near Ultraviolet Lasing From an Optically Pumped GaN Film Grown on Sapphire", X.H. Yang, T.J. Schmidt, W. Shan, J.J. Song, and B. Goldenberg, *Appl. Phys. Lett.* **66**, 1, (1995).

"Pressure-dependent Photoluminescence Study of Wurtzite GaN", W. Shan, T.J. Schmidt, R.J. Hauenstein, J.J. Song and B. Goldenberg, *Appl. Phys. Lett.* **66**, 3492, (1995).

"Hot-Phonon Generation in GaAs/Al_xGa_{1-x}As Superlattices: Observations and Implications on the Coherence Length of LO Phonons", D.S. Kim, A. Bouchalkha, J.M. Jacob, J.J. Song, J.F. Klem, H.Hou, C.W. Tu, and H. Morkoc, *Phys. Rev. B* **51**, 5449 (1995).

"Eu-Doped CaF₂ Grown on Si(100) Substrates by Molecular Beam Epitaxy", X.M. Fang, T. Chatterjee, P.J. McCann, W.K. Liu, M.B. Santos, W. Shan, and J.J. Song, *Appl. Phys. Lett.* **67**, 1891 (1995)

III. Major Accomplishments

1. Room temperature optically pumped lasing in GaN based epifilms and heterostructures

We have explored the optical properties of GaN based heterostructures with concentration on optically pumped stimulated emission and laser action in the GaN/AlGaN separated confinement heterostructures (SCH).

1.1. Optically pumped stimulated emission and lasing of MBE GaN/AlGaN SCH on sapphire and MOCVD GaN/AlGaN SCH on SiC

Optically pumped laser actions have been successfully achieved in AlGaN/GaN SCH grown on sapphire by MBE and similar structure on SiC by MOCVD. The laser actions in both kinds of samples were obtained at room temperature using a side-pumping geometry on small bar-like samples. The laser emission threshold was found to be $\sim 90 \text{ kW/cm}^2$ for the MBE SCH/sapphire and 65 kW/cm^2 for the MOCVD SCH/SiC. These values represent an order of magnitude of reduction of threshold value over that observed in thick uniform GaN epitaxial films ($\sim 800 \text{ kW/cm}^2$). High-finesse longitudinal lasing modes could be clearly observed from the MOCVD SCH/SiC with cleaved sample edge facets. We are the first to observe SE and lasing in SCH structures. The work on MBE GaN/AlGaN SCH samples has been published in **Applied Physics Letters**. The results from MOCVD SCH samples have been presented in various conferences and published in **SPIE Proceedings**. We attributed the significant reduction of the observed threshold values to the carrier confinement and waveguide effects of the SCH structures.

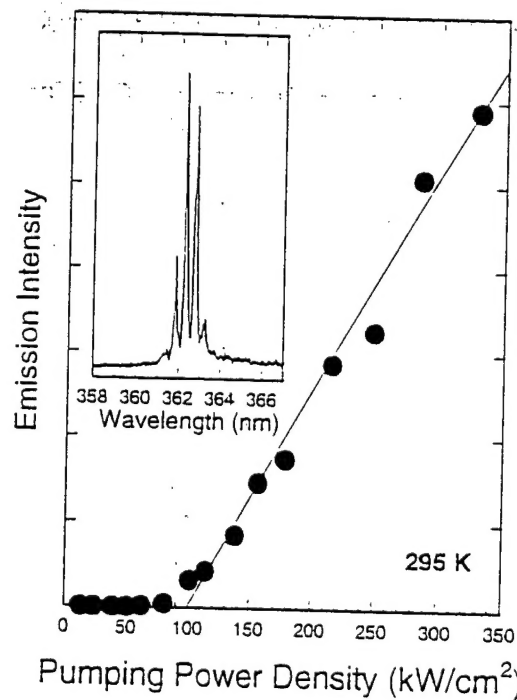


Fig. 1. Optical pumped stimulated emission intensity as a function of excitation power density for the SCH structure grown on SiC substrate. The inset shows the lasing modes.

1.2. Facet edge preparation for MOCVD GaN on Sapphire

We systematically studied the effects of facet edge preparation on stimulated emission and lasing. The specimens used in the optical pumping experiment were bar-like pieces merely cut off rather than cleaved from the large GaN wafer due to the well-known difficulties of forming high quality facets in sapphire. However, with attempts to finesse the cut surfaces, we did observe some substantial improvements in terms of Fabry-Perot cavity mode fringes. Lasing spectra taken under almost the same pumping conditions from the specimens subjected to different treatments demonstrated a progressive improvement of the quality of observed mode fringes. The spectra exhibited line-width narrowing and mode fringe enhancing, after the specimen's facet edges were fine polished. When a set of external mirrored cavity was attached to the samples, the mode quality was much improved. In addition, the emission intensity was found to increase by a factor of two. The results have been presented in several international conferences and topical workshops and published in **SPIE Proceedings**.

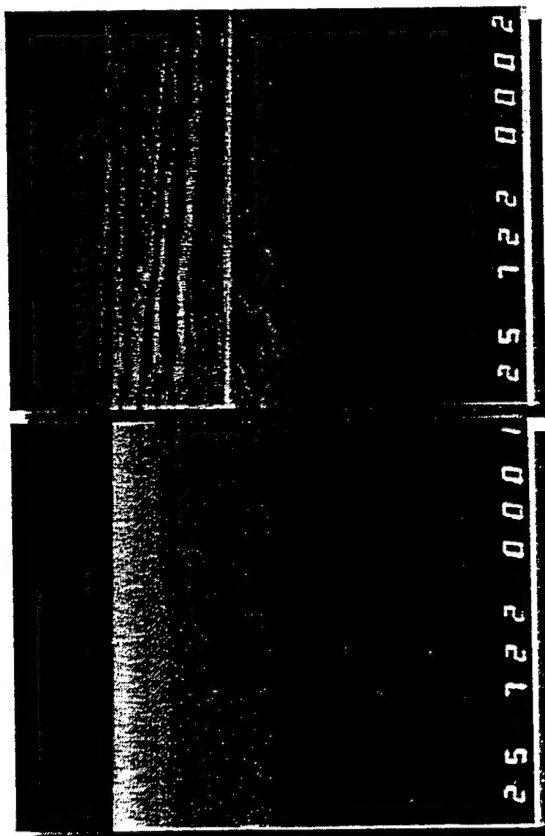


Fig.2. The SEM images of a GaN sample edge surface: after cut without mechanical polishing (upper portion); after fine mechanical polishing (lower portion).

2. Dynamics of photoexcited carriers in GaN

It is known that many aspects of device operation are governed by carrier dynamics, and the understanding of the recombination dynamics of carriers is of fundamental importance to the development of practical electroluminescence devices. Time-resolved luminescence spectroscopy was performed to study the dynamics of the photoexcited carriers. In this study, the primary excitation source used in this work was a pulsed dye laser synchronously pumped by a frequency-doubled modelocked Nd:YAG laser(76 MHz). The output frequency from the dye laser could be tuned by using different dyes. The output pulse with duration of less than 5 ps was then frequency doubled into UV range using a nonlinear crystal. The luminescence signals were dispersed by a monochromator and detected by a synchronscan streak camera with a temporal resolution of 2 ps. The overall time resolution of the system is less than 15 ps.

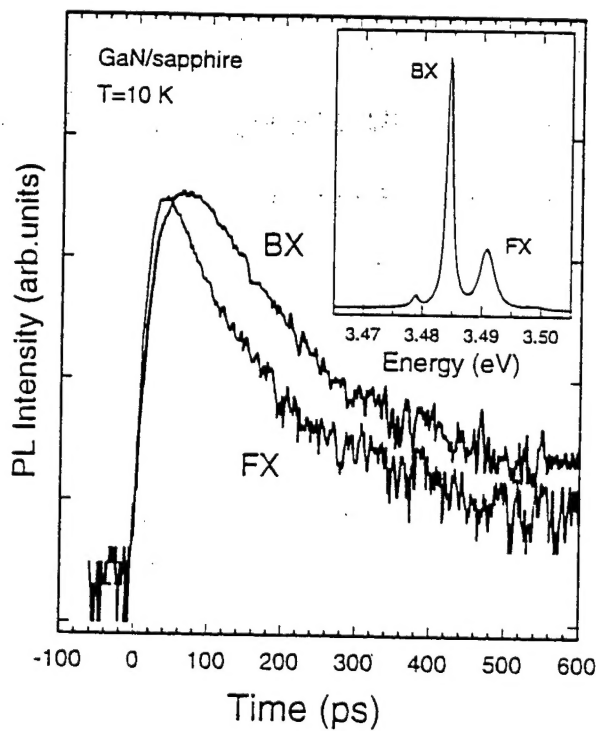


Fig.3. Temporal evolution of free-exciton and bound-exciton luminescence of a GaN sample at 10 K. The inset shows the time-integrated photoluminescence spectrum taken at the same temperature.

Time-resolved transient luminescence spectroscopy were performed to study the exciton radiative decay in various samples including GaN and InGaN epifilms, as well as GaN/AlGaN heterostructures. The decay time for both free-exciton and bound-exciton emissions was found to be quite short compared to the theoretically estimated radiative lifetime. The measured PL decay time for intrinsic free excitons and excitons bound to neutral donors is around 30-40 ps and 40-55 ps, respectively, while the theoretical estimated the radiative lifetime is in the proximity of a few tens of nanoseconds for free exciton and about one nanosecond for bound excitons. The results suggest that the lifetime of excitons in the GaN samples is governed by nonradiative recombination. The capture of excitons and trapping of carriers at defects and/or impurities through nonradiative relaxation processes dominate the decay of the exciton population. The capture process depends on the density of impurities and defects in the GaN samples. However, the PL decay in InGaN alloys for localized excitons in the alloys was found to be at least an order of magnitude longer than that for pure GaN.

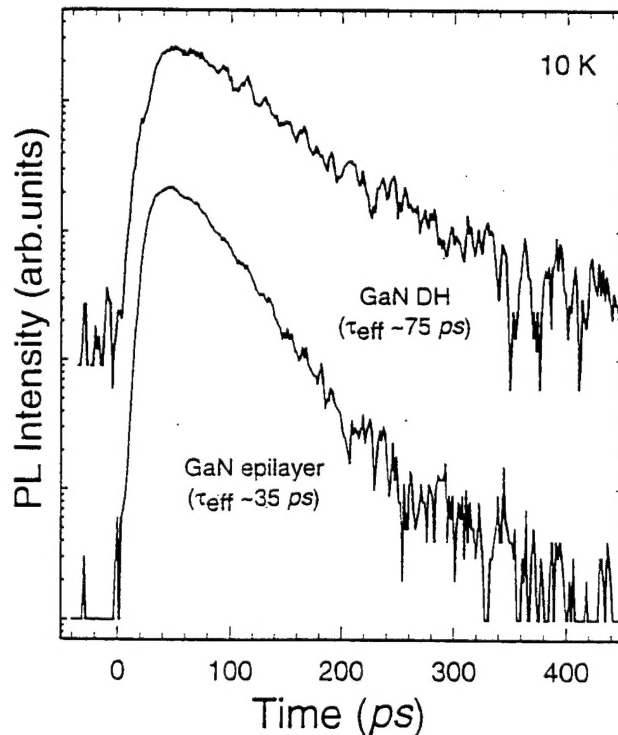


Fig.4. Comparison of the time decay of the exciton luminescence between a bulk-like GaN epilayer and a GaN active layer in a DH structure.

We have also made a comparative study of the time decay of exciton luminescence in GaN/AlGaN double heterostructures (DH) and GaN epitaxial layers. The time evolution of bound-exciton emission observed in a GaN/AlGaN DHS sample was compared with that in a GaN epitaxial film. Both samples were deposited on SiC substrates under very similar growth conditions except that the DH structure was grown on one of them. The Al concentration of the AlGaN cladding layers is about 7%. In this study, the excitation photon energy was tuned very close to the band gap of the GaN to directly generate excessive carriers in the GaN active layer so that diffusion of carriers from AlGaN cladding layers into active layer can be avoided.

The measured decay time for the bound exciton emission in the DHS sample was found to be (~74 ps) two times longer than that in the bulk-like GaN (~37 ps). It is known that in a strained heterostructure system such as AlGaN/GaN, the built-in strain within the uniform elastic limit can significantly reduce the density of defects, such as dislocations. The increase in the exciton PL decay time observed in the DHS sample implies that the AlGaN cladding layers with a small mole fraction could be relatively effective in reducing the density of dislocations in the GaN active layer. In addition, the deposition of cladding layer on the top of the GaN active layer could have passivated the surface states resulting in a reduction of the nonradiative recombination velocity of the photoexcited carriers on the bare surface and in its vicinity. This is one of several important issues currently under investigation in our group. These results were presented in a number international conferences and have been published.

3. Picosecond Degenerate Four-wave Mixing in GaN

We have initiated the study of optical nonlinearity in GaN. Degenerate wave mixing experiments were performed for the first time using frequency-doubled pulses from a mode-locked, Q-switched Nd:YAG laser operating with a repetition rate of 10 Hz. The second harmonic output of the laser with a 13 ps pulse duration was equally split in energy into two pump beams and one probe beam. These beams were spatially and temporally recombined in the samples in a forward propagating boxcar geometry. The excitation wavelength is 532 nm, corresponding to the excitation photon energy well below the band gap of GaN. The patterned diffracted higher order wave-mixing signals in the phase-matching directions could be clearly visible to human eyes. The strong diffracted signals in this wide band-gap material are consistent with the elegant band charge model, which predicts higher nonlinearities as the material becomes more polar. The intensity and time response of the scattering efficiency in GaN was studied. By delaying the arrival of the probe pulses relative to the pump pulses, the response of the nonlinear optical changes such as scattering efficiency in the GaN sample was studied. Intensity dependence of the observed signal suggests carrier generation by both single and two photon effects. An effective nonlinear refractive coefficient, with the value of $1 \times 10^{-3} \text{ cm}^2/\text{GW}$ was derived for the effective nonlinear refractive index n_2 for GaN. Time response of the wave-mixing

signal was found to be dictated by carrier lifetimes. This work opens a new area of research and applications for GaN-based samples and results have been published in **Applied Physics Letters**.

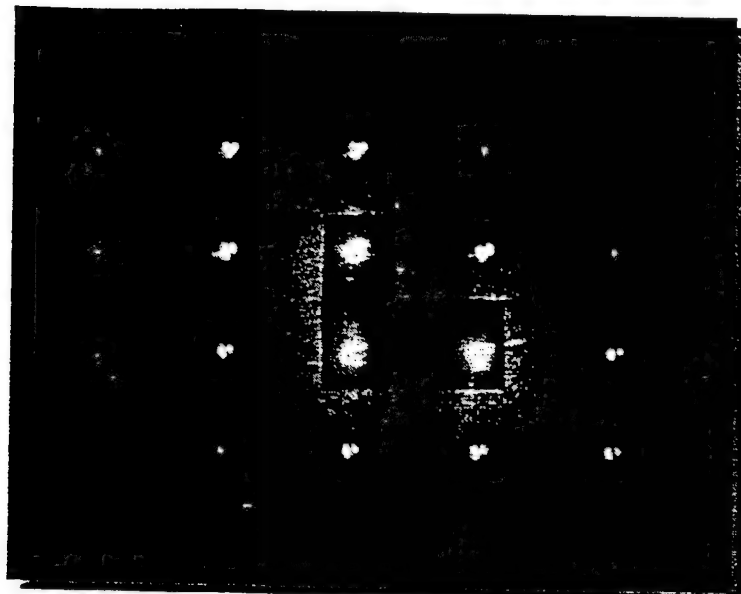


Fig.5. Photograph of the wave mixing signals showing three attenuated pump and probe beams and the higher order nonlinear diffracted signal spots. The laser photon energy (2.33 eV) is well below the room-temperature GaN band gap.

4. Strain effects on exciton transitions in GaN

In the studies of the strain effects on the fundamental optical processes in GaN materials using spectroscopic methods combined with X-ray diffraction measurements, the exciton transitions with lower energies were observed in GaN grown on SiC, and with higher energies for the same transitions for GaN grown on sapphire, in comparison to those obtained from string-free bulk GaN. Our results suggest that residual strain in GaN epilayers resulting from lattice-parameter and thermal-expansion mismatch plays an important role in determining the precise exciton transition energies.

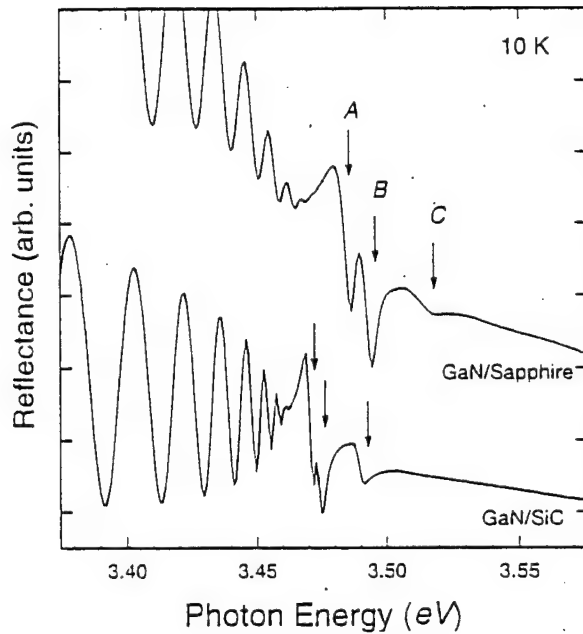


Fig.6. Reflectance spectra of the exciton transition region of GaN samples grown on SiC and sapphire at 10 K.

X-ray diffraction measurements were performed to determine the variations in the lattice parameters of GaN epilayers on SiC and sapphire, respectively. Our results clearly indicate that GaN epilayers grown on SiC exhibit basal tensile strain, while those on sapphire substrates are under biaxial compression. Based on those results, the values of the four principal deformation potentials of wurtzite GaN have been determined. Our results yield the uniaxial deformation potentials $b_1 \approx -5.3$ eV and $b_2 \approx 2.7$ eV, as well as the hydrostatic components $a_1 \approx -6.5$ eV and $a_2 \approx -11.8$ eV. A report on these results has been accepted to publish in Phys. Rev. B15.

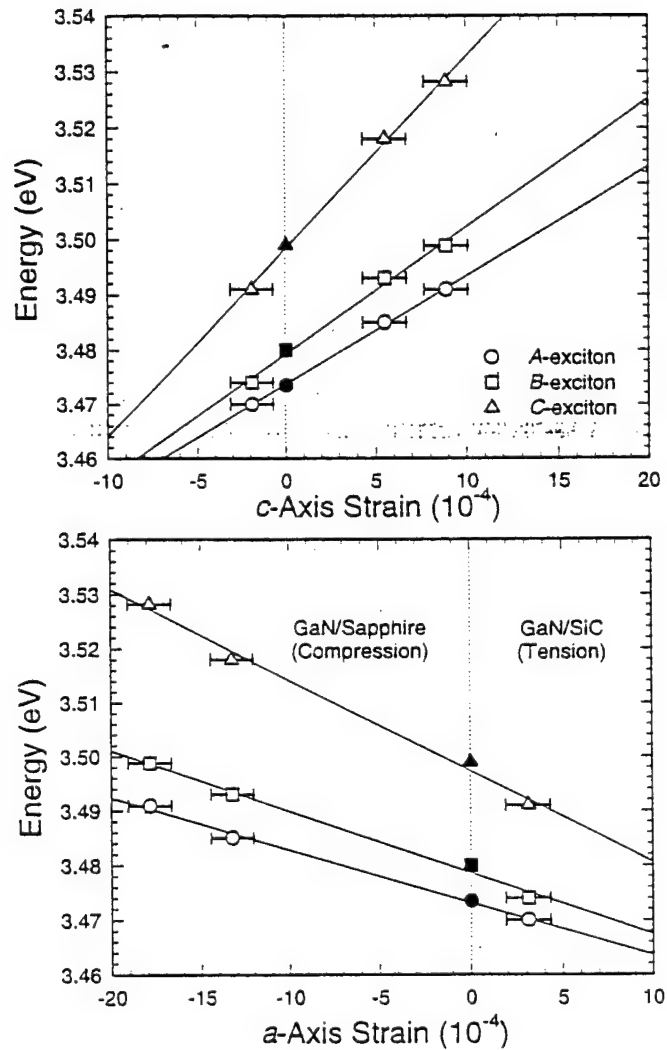


Fig.7. The measured excitonic transition energies from GaN samples as a function of relative in-plane (biaxial) strain (lower portion) as well as the relative strain along c-axis (upper portion). The exciton transition energies of strain-free GaN were included for reference. The solid lines are the best linear fits to the experimental data. Four principal deformation potentials for the wurtzite GaN were derived from the fits.

5. GaN exciton binding energy determination

We carried out an experimental study on the binding energy for intrinsic free excitons in wurtzite GaN. High-quality single-crystal GaN films grown by metalorganic chemical vapor deposition were used in this study. Various excitonic transitions in GaN were studied using reflectance measurements. The observation of a series of spectral features associated with the transitions involving the ground and excited exciton states allowed us to make a straightforward estimate of exciton binding energy using the hydrogenic model. Our results yielded a binding energy $E_b = 0.021 \pm 0.001$ eV for the A and B excitons, and 0.023 ± 0.001 eV for the C exciton in wurtzite GaN within the framework of the effective mass approximation. (See Fig. 8.)

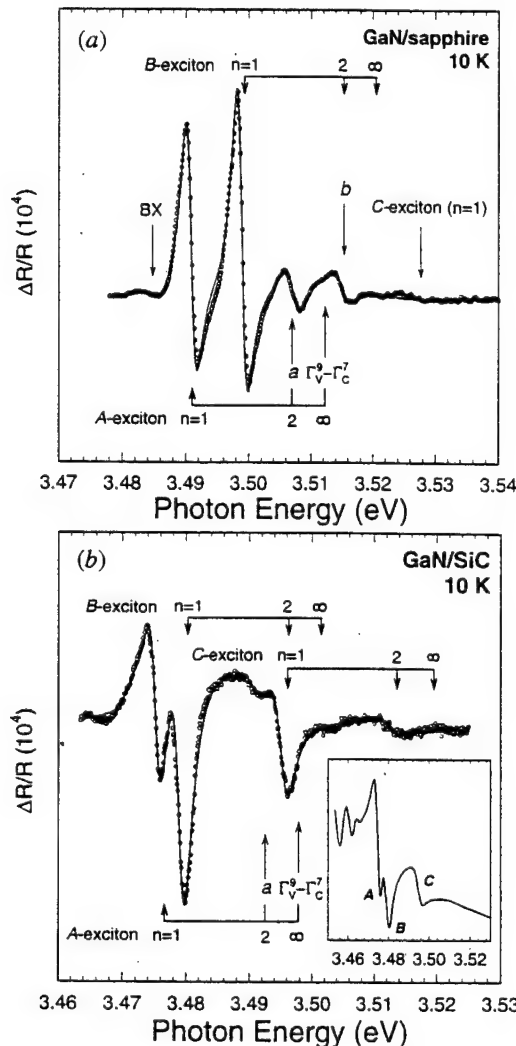


Fig. 8. 10-K PR spectrum taken from the $7.2\mu\text{m}$ GaN/sapphire (a) and a $3.7\mu\text{m}$ GaN/SiC (b). Open circles are experimental data, and solid lines represent the best result of the least-squares fit to the data. The identifications of the various spectral features are given by the notations.

6. Optical transitions in $\text{In}_x\text{Ga}_{1-x}\text{N}$ alloys

We performed optical studies of $\text{In}_x\text{Ga}_{1-x}\text{N}$ alloys ($0 < x < 0.2$) grown by metalorganic chemical vapor deposition on top of thick GaN epitaxial layers with sapphire as substrates. Photoluminescence (PL) and photoreflectance measurements were performed at various temperatures to determine the band gap and its variation as a function of temperature for samples with different indium concentrations. Carrier recombination dynamics in the alloy samples were studied using time-resolved luminescence spectroscopy. While the measured decay time for the alloy near-band-edge PL emissions was observed to be generally around a few hundred picoseconds at 10 K, it was found that the decay time decreased rapidly as the sample temperatures increased. This indicates a strong influence of temperature on the processes of trapping and recombination of excited carriers at impurities and defects in the InGaN alloys. (See Fig. 9.)

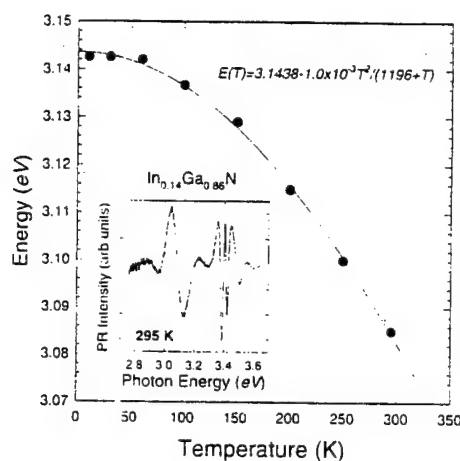


Fig. 9. Temperature dependence of interband transitions energy of the $\text{In}_{0.14}\text{Ga}_{0.86}\text{N}$ sample. The solid curve represents least-squares fits to the experimental data using Varshni empirical equations. The inset shows a room-temperature PR curve of the sample.

7. Femtosecond four-wave-mixing in GaN in the excitonic range

We carried out, to our knowledge, the first femtosecond degenerate four-wave-mixing (FWM) studies on nearly homogeneously broadened excitons in high quality GaN epilayer samples. Spectrally-resolved (SR) FWM data were dominated by the A and B intrinsic excitonic resonances. SF-FWM, combined with time-integrated (TI) FWM, demonstrated that the excitonic resonances were nearly homogeneously broadened even at low temperatures. The temperature dependent dephasing rate was used to deduce exciton-phonon interaction rates. TI-FWM showed a strong beating between the A and B excitons,

and the beats were shown to be true quantum beats. In addition, a 180° phase shift in the quantum beating was when the polarization geometry was changed from collinear to cross-linear. (See Fig. 10.)

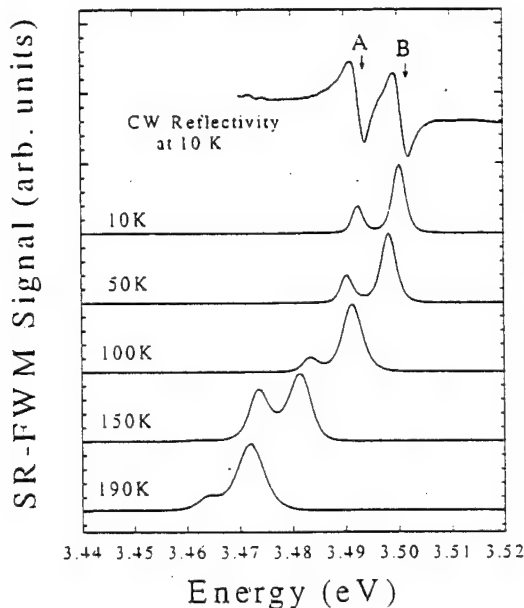


Fig. 10. Spectrally-resolved (SR) FWM signals from the A and B exciton resonances near zero delay at 10, 50, 100, 150, and 190 K plotted together with CW reflectivity data from the same sample. Different temperatures are vertically displaced for clarity.

8. Cubic GaN on GaAs (100) by ECR-MBE

By December, 1993, all of the major capital equipment items which constitute the upgrade to nitride growth capability of our conventional solid-source arsenide-based III-V MBE system were received. By May, 1994, the upgrade was successfully implemented, and we were able to attempt our first ECR-microwave-plasma-assisted MBE (ECR-MBE) growth of nitrides. Briefly, our nitride MBE system consists of a Superior Vacuum Technology (SVT) III-V growth system which has been retrofitted with a Wavemat Model MPDR 610iA ECR microwave source, a CTI Cryogenics CT-8 cryopump and gate valve, and a pair of effusion source ovens for n- and p-type doping. Column III (Ga, Al, In) and dopant (Si, Mg) fluxes are produced by means of conventional effusion ovens while the nitrogen is introduced in the form of a nitrogen-containing gas via a controlled leak through the ECR source into the ultrahigh vacuum (growth) chamber. Because of the high equilibrium vapor pressure of N₂ over GaN, activation of the N-containing species via the ECR source is necessary for nitride growth. In our system, ultrahigh purity N₂, post-filtered for oils and water vapor with the use of a Nanochem purifier, and for particulates by means of a Matheson filter, is introduced into the MBE growth chamber through an all-stainless steel manifold which is capable of being purged, and also, evacuated, via the MBE system roughing line. Initial operational tests were performed to optimize the ratio of forward to reflected microwave power of the ECR source, and then, to establish the forward power thresholds for plasma ignition and extinction, respectively, at a fixed set of pressures in the range from $\sim 8 \times 10^{-5}$ to 8×10^{-4} Torr.

a. MBE Growth

Once the operational characteristics of our new ECR source were established, an initial series of six GaN films was grown. The purpose of these initial growth runs was to determine suitable values for the relevant MBE growth parameters, and to assess their effect on GaN growth rate, surface morphology, and crystal structure. The following three growth parameters directly affect the ECR-MBE growth of GaN films: microwave forward power, substrate temperature, and Ga flux. GaAs (100) was chosen as the initial substrate for growth since atomically clean starting surfaces, through MBE growth of a GaAs buffer layer, could readily be achieved, thereby greatly reducing complications in GaN growth due to starting-surface imperfections. All samples were grown according to the following procedure: (i) a $\sim 1\text{mm}$ GaAs buffer layer was grown at 600°C ; (ii) the growth chamber was stabilized to a N₂ partial pressure of 2×10^{-4} Torr and nominal flow rate of ~ 10 sccm with the GaAs substrate held at 580°C in an As₂ flux; then, in rapid sequence: (iii) the N₂ plasma was ignited, (iv) the As₂ flux was shuttered closed, and (v) the Ga flux was shuttered open. This procedure, and subsequent growth observations, are similar to those reported by Morkoc and co-workers, though in our case, on-axis, rather than vicinal GaAs (100) substrates were used. This difference resulted in the discovery of GaN surface reconstructions which have not previously been reported, to our knowledge, which may provide valuable clues regarding the initial stages of

epitaxial growth of GaN. The relevant growth parameters are summarized in the following table:

Table I. Summary of MBE growth parameters for GaN on GaAs (100).

Sample ID	P _{fwd} (W)	T _w (°C)	Ga Flux (GaAs ML/s)	t _{dep} (h)	Expected Thickness (Å)
OS94.004	75	620	0.05	6.25*	1500
OS94.005	75	620	0.16	2.23*	1500
OS94.006	80	620	0.05	8.23*	2000
OS94.007	100	620	0.05	9.56	2400
OS94.008	100	620	0.10	8.00	3800
OS94.009	100	620	0.16	5.38*	3800

*Limited by loss of stoichiometry

Following Morkoç, an initial layer of GaN ($\sim 100 \text{ \AA}$) was grown for 30 min at a slightly reduced temperature (580°C) in a Ga flux of 0.05 GaAs-equivalent monolayers/sec (e-ML/s); the remainder of each film was then grown at 620°C using the Ga flux shown in the table. As can be seen from the table, the substrate temperature was held constant while microwave power and Ga arrival rate were deliberately varied. Anticipating plasma-induced microstructural damage in our films, our strategy was to determine the minimum value of microwave power which is consistent with stable plasma operation, and, for this power level, to determine the maximum Ga flux at which stoichiometric growth could be maintained. Forward power levels were determined from the microwave power supply readout, and Ga flux, shown in Table I in terms of equivalent monolayer growth rate for GaAs (assuming Ga arrival-rate-limited growth), was calibrated through the use of reflection high energy electron diffraction (RHEED) oscillation measurements performed during the growth of each GaAs buffer layer. The thicknesses which appear in Table I have been estimated on the assumptions of: Ga arrival-rate-limited growth, unity sticking coefficient of Ga, and a zinc blende GaN crystal structure. In this case, a table entry for the Ga flux of 0.05 e-ML/s corresponds to a 250 Å/h GaN growth rate.

b. RHEED Characterization

RHEED measurements were performed *in situ* during each GaN growth run, and tended to exhibit a similar sequence of patterns in each instance. A typical sequence of RHEED patterns is shown in Fig. 11. Figure 1(a) shows the (2 x 4) reconstruction of the GaAs buffer layer, which served as the starting surface for each GaN growth. Immediately after the plasma is struck, the pattern shifts to the streaked pattern shown in Fig. 11(b). As will be discussed below, we believe that this pattern corresponds to nitridated GaAs surface, or, equivalently, to a single monolayer of GaN on GaAs, and, based upon the streak spacing, that this GaN monolayer appears to be coherently strained to the GaAs substrate. The qualitative appearance of the pattern in Fig. 11(b) (sharp streaks) indicate an epitaxial surface which is both flat and single-crystal. Next, Fig. 11(c) shows the emergence of a

somewhat spotty pattern (intensity modulation of streaks along the growth axis) after only approximately 1 min of GaN deposition. The appearance of spots indicates three-dimensional growth (islanding) of the GaN layer. Also faintly visible in this image are $n=\pm 1$ orders of the GaAs substrate, implying incomplete coverage by the GaN film of the GaAs surface, which is consistent with the GaN material "balling" into islands. Next, in Fig. 11(d), the spotty GaN pattern becomes streakier, and the first indications of a GaN surface reconstruction is revealed through the presence of $n/2$ -order streaks. This was observed after approximately 11 min of GaN growth. As more GaN is deposited, the GaN diffraction pattern becomes progressively sharper and streaked, consistent with an increasingly two-dimensional GaN epitaxial growth surface as GaN islands begin to coalesce. Finally, Fig. 11(e) shows the RHEED pattern after 7.7 h of deposition and an estimated thickness of approximately 2000 Å.

In addition to qualitative information regarding crystal structure and surface morphology, analysis of the streak spacings permit quantitative analysis of surface lattice constants at various stages during MBE growth. Figure 12 shows intensity linescans for the RHEED data considered in Fig. 11. These data were obtained by digitizing our RHEED photos with the use of a CCD camera which was hardware-interfaced to a computer via a frame grabber, and then, by plotting the light intensity vs. pixel position of a horizontal row of pixels for each photo in Fig. 11. (The digitization was performed at Caltech; we are in the process of setting up a similar capability at OSU, under partial support of this program.) To facilitate comparison of lattice constants, the abscissa values are normalized to the bulk surface reciprocal lattice constant value of the GaAs substrate. In Fig. 12, peak spacing is inversely proportional to the real-space surface unit cell length. The dotted curve corresponds to the (2 x 4) reconstruction of an As-stabilized GaAs (100) surface, where, in this case, the RHEED azimuth is that which corresponds to the appearance of $n/2$ -order streaks, as can be read directly off the abscissa. Curve A appears almost immediately (<1 sec) after the N₂ plasma is ignited. This transition occurs with or without exposure to the As flux, and apparently corresponds to the replacement of the top monolayer of As by N on the growth surface. This is consistent with the stronger Ga-N chemical bond strength in comparison with the Ga-As bond. It is significant to note that the peak spacings of curve A are *commensurate* with those of the substrate. This indicates that the nitridated GaAs surface, or, alternatively, a single monolayer of GaN, is *coherently strained* to the GaAs substrate. Furthermore, this RHEED pattern does not change until the Ga flux is turned on. In addition, the pattern is stable even when the column V (As or N-plasma) fluxes are removed, demonstrating that re-evaporation of surface N from GaN is negligible at our typical growth temperatures (~600°C), *unlike* the case for column-V species under conventional arsenide or antimonide MBE growth conditions, where surface stoichiometry can be maintained only in the presence of the As or Sb flux, respectively. The $n/3$ -order peak spacings seen in curve A of Fig. 12 have not been reported previously, and suggest the discovery of a new surface reconstruction for strained GaN (100).

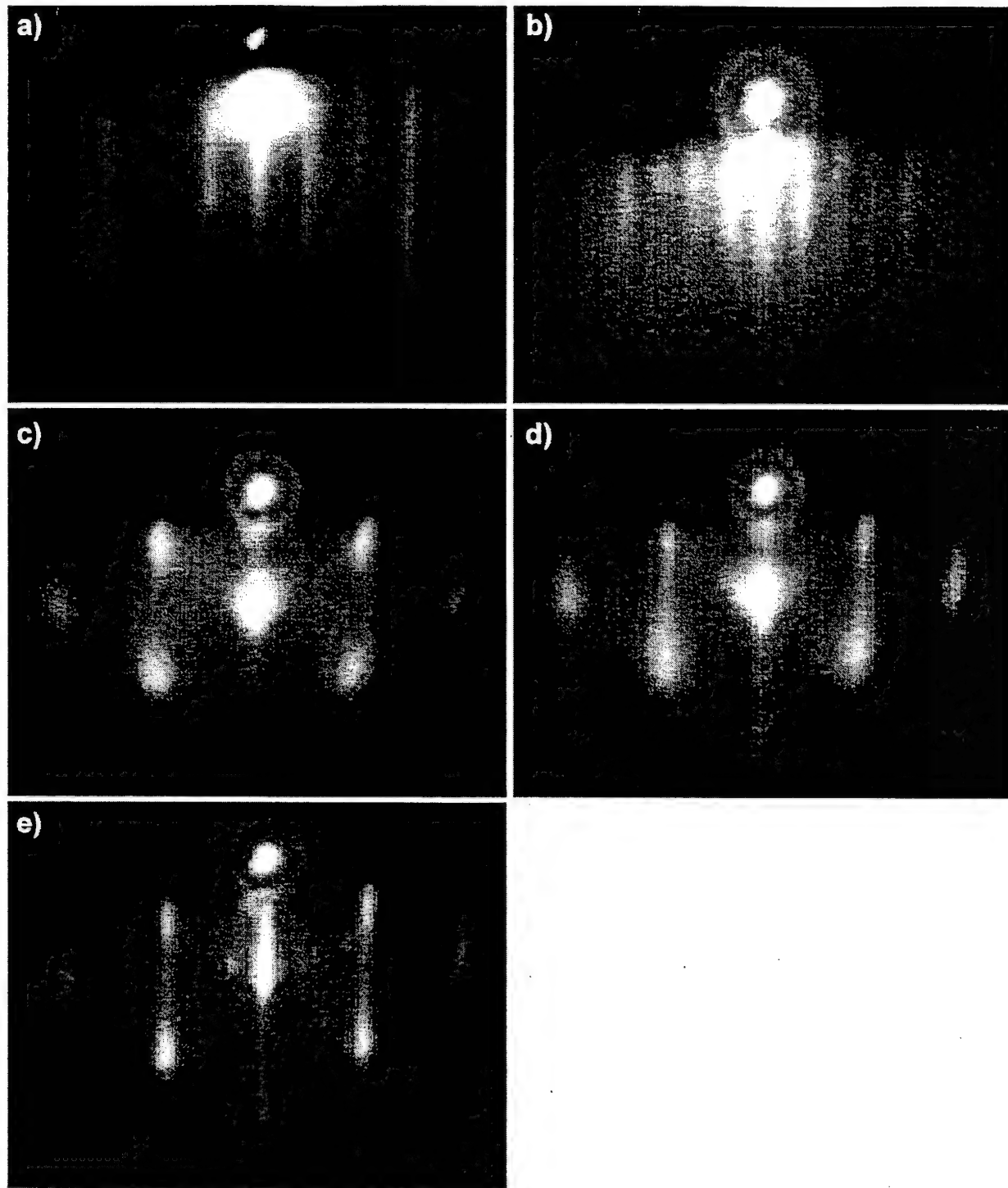


Fig. 11. Typical RHEED pattern evolution for growth of zinc blende GaN on GaAs (100). [110]-azimuthal data are shown for sample OS94.006; other growth runs are similar. Pictured are (a) GaAs buffer layer (2×4) reconstruction; GaN after deposition times of: (b) <1 s; (c) 1.5 min; (d) 11 min; (e) 7.6 h.

RHEED PROFILE vs. GaN DEPOSITION TIME
FOR GROWTH ON GaAs (100)

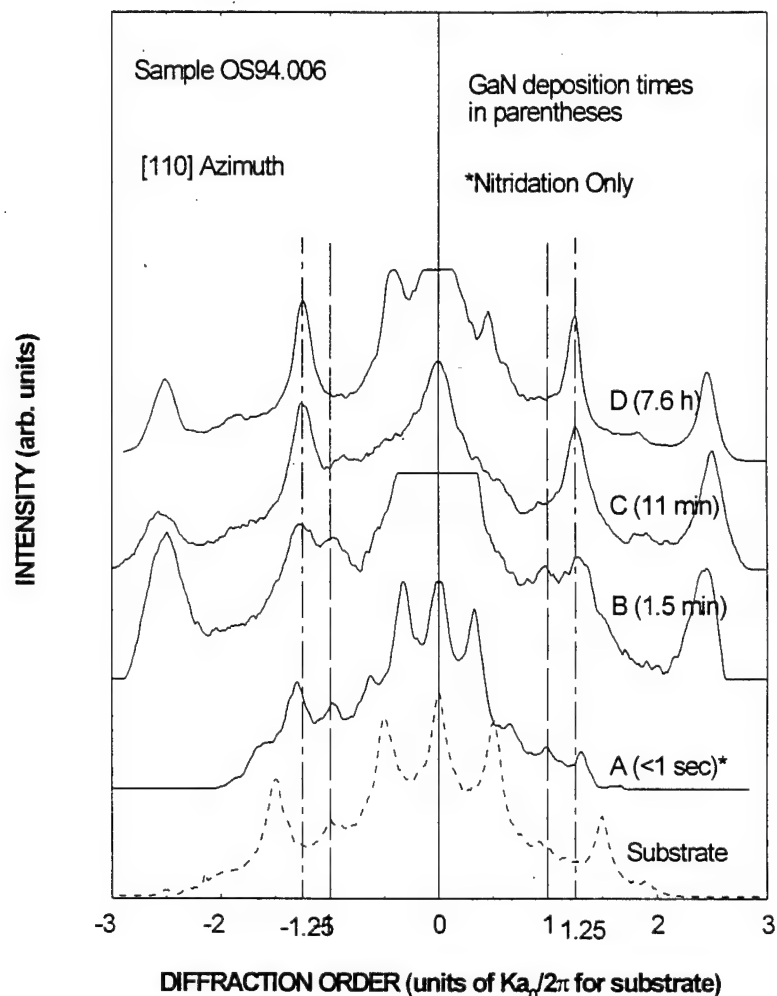


Fig. 12. Linescans for RHEED data shown in Fig. 11. Dotted: GaAs substrate; solid: GaN, after indicated deposition time.

Once the Ga flux is turned on, the RHEED pattern quickly becomes spotty, and changes in peak spacing. Comparison of curves B thru D in Fig. 12 reveals that very soon (approximately 6 Å) into the growth of GaN on GaAs (100), the GaN relaxes in lattice constant to its bulk value for the zinc blende phase (approximately 25% smaller than that of GaAs). The alignment of the $n=\pm 1$ peaks of stress-relaxed GaN (curves B thru D) is indicated in the figure. The corresponding lattice constant, $a = (5.65 \text{ \AA})/1.25 \gg 4.5 \text{ \AA}$, is identical to the value determined by x-ray diffraction (XRD) below. The numerical value of lattice constant, as well as the qualitative pattern of diffraction spots seen, for example, in Fig. 11(c), are both consistent with the *zinc blende* phase of GaN, as expected for epitaxial growth on GaAs (100). Also present in curve B of Fig. 12 are the $n=\pm 1$ peaks of GaAs, which are absent in curves C and D. As explained above, this is consistent with the exposure of GaAs patches on the surface after the initial onset of islanding of GaN, whereas once the

GaN islands grow sufficiently that they begin to coalesce, no exposed GaAs surface remains.

9. Nitridation of GaAs (100)

a. GaN formation through nitrogen plasma exposure of GaAs

In a series of surface-nitridation experiments of the GaAs (100) surface with an ECR-microwave plasma, we have shown here and under support of our companion AASERT programs that prolonged nitridation of the surface actually results in the formation of GaN (100). This was deduced directly from comparison of real-time RHEED observations during timed nitridations of GaAs, and RHEED data taken from deposited GaN films on GaAs, as shown below in Fig. 13.

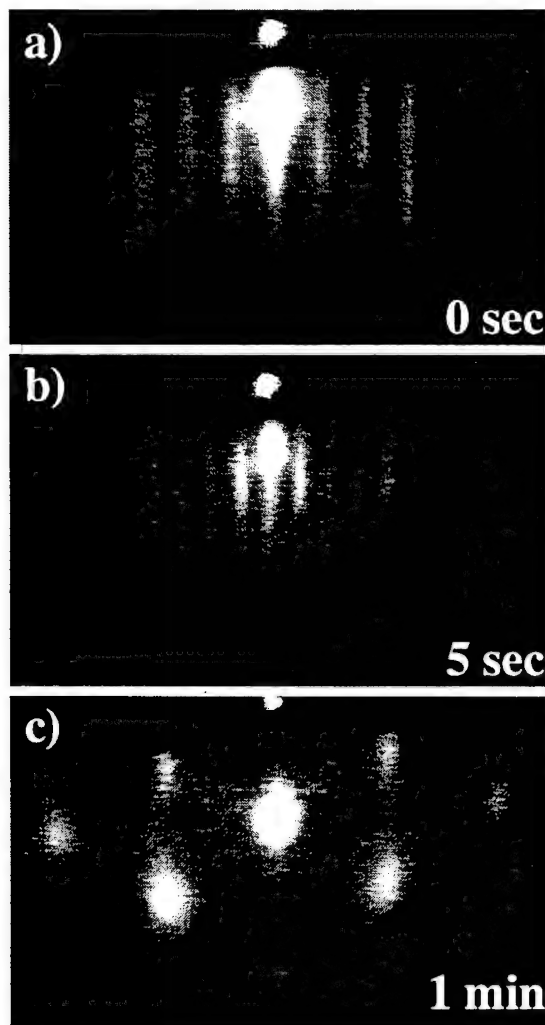


Fig. 13. RHEED data of an initially As-stabilized GaAs (001) surface as a function of nitrogen plasma exposure time. (a) 0 sec; (b) 5 sec; (c) 1min.

Comparison with the RHEED data from the nitridation sequence (Fig. 13) with the deposition series (Fig. 11 earlier) reveals that similar processes are operative during the initial stages of GaN epitaxy on GaAs, and during surface nitridation of GaAs.

Additionally, comparison of Fig. 13(c) with the RHEED images of Fig. 11 clearly indicate that prolonged (1 min) nitridation of GaAs (100) results in the formation of zinc blende GaN. This is interpreted as the result of an “anion-exchange” process involving replacement of initially surface (upon brief plasma exposure) and eventually sub-surface (for prolonged exposure) As with N atoms. This is entirely consistent with the greater thermodynamic stability of the Ga–N over the Ga–As bonds at the substrate temperature (~600°C).

b. Identification of microscopic processes and kinetics

Further experimentation revealed that the RHEED transition depicted in Figs. 13(a) and (b) is actually reversible. Near 600°C, the characteristic As-stabilized (2x4) GaAs surface reconstruction [Fig. 13(a)] upon N* exposure immediately changes to the *specular* (3x3) pattern depicted in Fig. 13(b). In addition, upon replacement of the N* flux with an As flux, the pattern again *returns* to the original (2x4) though *much more slowly* than the forward reaction. We were the first to observe and report this behavior. Our published work has shown that the observed RHEED pattern changes correspond to surface-layer anion exchange of N and As species, for sufficiently brief (< 8-10 s) N* exposure times. In contrast, we have shown that longer exposure times (up to 1 min) result in the formation strain-relaxed islands of zinc blende GaN. Together, these observations suggest a *nitridation* of the As-terminated GaAs surface due to incident N* flux such that first rapid surface, followed by slower subsurface, anion exchange processes, take place.

RHEED PATTERN EVOLUTION vs. INCIDENT FLUX ON GaAs (100)

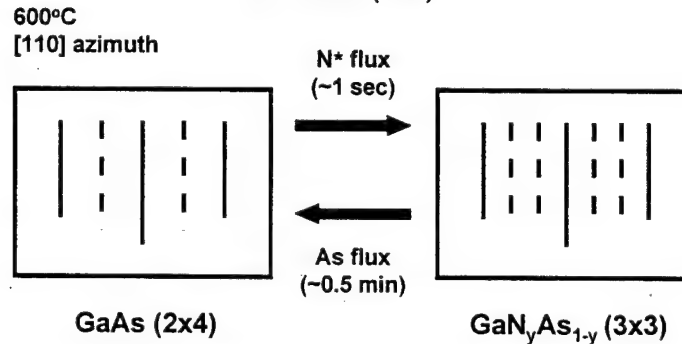


Fig. 14. RHEED Pattern evolution under N^{*} and As fluxes. Note time scales. GaNAs pattern is commensurate with the substrate. Reaction is reversible, if N^{*} exposure time is limited to a few sec.

The RHEED pattern dynamics have also been examined quantitatively through time-resolved measurements. The pattern evolution is quantitatively assessed as a function of time through intensity of the 1/3-order reconstruction line. This line, present in the (3x3), but absent from the (2x4) pattern, is taken as a measure of the extent of surface reaction. Assessment of the (3x3) onset and decay are presented in Fig. 15(a). From the inset, it is seen that the presence (absence) of As flux has negligible effect on the rate of surface nitridation (N-for-As replacement), and that the time scale for nitridation is ~1 s. In contrast, the surface, once nitrided, is quite stable, even when all fluxes are removed. Note that the time scale for decay of the

(3x3) pattern is *much* longer than that of As-terminated GaAs (2x4) at similar temperature. This result suggests strongly that the (3x3) pattern is primarily associated w/ a N-terminated surface.

GaN (3x3) ONSET AND DECAY

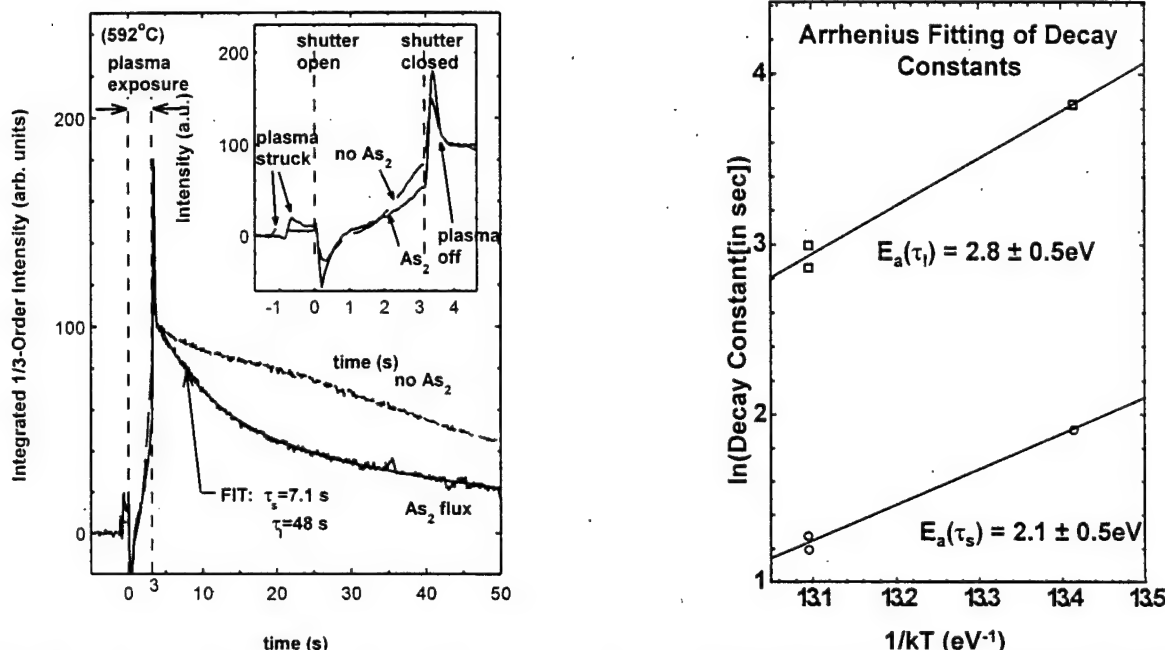


Fig. 15. (a) 1/3-order RHEED streak intensity decay, corresponding to N desorption from the (3x3) nitrided surface. Decay rates are approximately exponential, as shown. (b) Temperature dependence of decay rates. Results suggest thermally activated processes, with activation energies indicated.

Decay of the (3x3) surface in the presence of an As flux is well described by a superposition of short and long exponential decay terms, as seen in Fig. 15(a). The corresponding lifetimes, τ_s and τ_i , respectively, each exhibit temperature-dependent behavior, as shown in Fig. 15(b). Assuming a Boltzmann-factor dependence, a preliminary assessment of thermal activation energies is possible. The results of this analysis are given in the figure. Considering the large difference in Ga-N and Ga-As bond strengths (heats of formation 6.81 and 5.55 eV respectively) compared to kT , the above results are consistent with thermally activated surface N or As desorption processes, with a much higher kinetic barrier present for the case of N desorption.

To better assess the physical structure which corresponds to the (3x3) reconstruction, we have taken advantage of our observation that a nitrided (3x3) surface can be overgrown commensurately with GaAs. Thus, in a series of experiments, we attempted to "bury" this unknown structure under a GaAs layer and to utilize high-resolution X-ray diffraction (HRXRD) of the resultant heteroepitaxial structure to enable a determination of alloy composition and strain associated with the (3x3) reconstruction.

10. GaNAs/GaAs SUPERLATTICES

a. HRXRD Studies

To elucidate the physical origin of the (3x3) reconstruction resulting from N-for-As anion exchange at a GaAs (100) surface as described above, a set of 36-period (to improve signal-to-noise) nitrided-ML/GaAs ($\text{GaN}_y\text{As}_{1-y}/\text{GaAs}$) superlattices was grown as a function of temperature and nitridation time on GaAs buffer layers by ECR-MBE; growth details are summarized in Table II. All other procedures and conditions were nominally held constant in order to minimize run-to-run variation of substrate temperature. Growth of each superlattice period in our structures involves: (i) N^* exposure without As_2 flux for the time shown in the table; (ii) immediate overgrowth of GaAs at ~ 0.75 ML/s for 100 s; (iii) an "As-soak" (As_2 flux only) for 30 s.

Table II. Indicated are growth temperature, temperature uncertainty, and plasma exposure time for each sample in the set. Uncertainties listed below indicate only reproducibility from run to run within the sample set

Sample Number	Substrate Temperature (°C)	Relative Uncertainty* (°C)	Plasma Exposure Time (sec)	Nitrided Layer Composition, y (%)
OS95.002	560	+/-5	4	16.5
OS95.003	570	+/-2	4	7
OS95.004	580	+/-5	4	4
OS95.005	550	+/-2	4	26
OS95.006	540	+/-5	4	26.5
OS95.009	550	+/-5	6	33

The HRXRD measurements were performed with the use of a Philips Materials Research Diffractometer (MRD) operated in the 4-crystal mode using (220) Ge reflections. Both $w/2q$ scans, and "area" scans (reciprocal-space mapping), about the substrate (004) and (115) Bragg peaks, respectively, are performed on each sample. Additionally, dynamical simulations of the $w/2q$ scans, to aid in compositional and strain profile analysis of our superlattices, are computed with the use of the Philips High Resolution Simulation (HRS) software package.

The resultant x-ray rocking curves, about the substrate (004) reflection, are presented in Fig. 16(a). All samples were grown under nominally identical conditions (4 s exposure), apart from growth temperature. (Scans for growth at 550 and 570°C have been omitted for clarity.) All samples are coherently strained, as confirmed through (115) area scans. Inspection of the figure clearly reveals a very strong dependence on growth temperature T of the epitaxial structure. Two-dimensional equivalent alloy compositions (y defined above) are determined from XRD peak

positions and verified through dynamical simulations; final results are summarized in Table II. Figure 16(b) shows an Arrhenius plot of the resultant ML alloy compositions. The results, within experimental error, clearly suggest two distinct regimes of behavior which act to limit N incorporation: (i) *dose-limited* (low-T); and (ii) *kinetically limited* (high-T). This finding suggests that a thermally activated N surface-segregation process, in addition to the thermally activated N desorption process found above from RHEED data, is active, and can be significant at typical GaN ECR-MBE growth conditions. Extracting an activation energy from the linear portion of the data yields a value which is greater than that found for the desorption processes alone from Fig. 15(b) above, consistent with the existence of an additional thermally activated process. We have developed a kinetic model to account for the observed results, which also quantitatively explains the increased composition observed for the 6 sec exposure (sample OS95.009); this kinetic model will be described in detail next.

b. Kinetic Modelling of Microscopic Processes

The pertinent experimental result from the above HRXRD results is the unusually strong dependence of N content (y in $\text{GaN}_y\text{As}_{1-y}/\text{GaAs}$ superlattices) on substrate temperature during growth. This behavior is in evidence in Fig. 16, which shows the order-of-magnitude variation in N content over a range of only 40°C of substrate temperature. As suggested by Fig. 16(b), a thermally activated process appears to be limiting the maximum N content available at high growth temperatures while at low temperatures this upper limit appears to be "dose"-limited by the plasma exposure time. As previously reported, the activation energy obtained from the data in Fig. 16(b) is in disagreement with the activation energy which we observe from RHEED studies of thermally activated N surface desorption, suggesting the presence of an additional, thermally activated mechanism. This led us to hypothesize the existence of a thermally activated N surface-segregation process (in addition to N desorption) during MBE growth. However, confirmation of the existence of this second process had to await the development of an analytical model of the microscopic growth processes with which to quantitatively test our hypothesis.

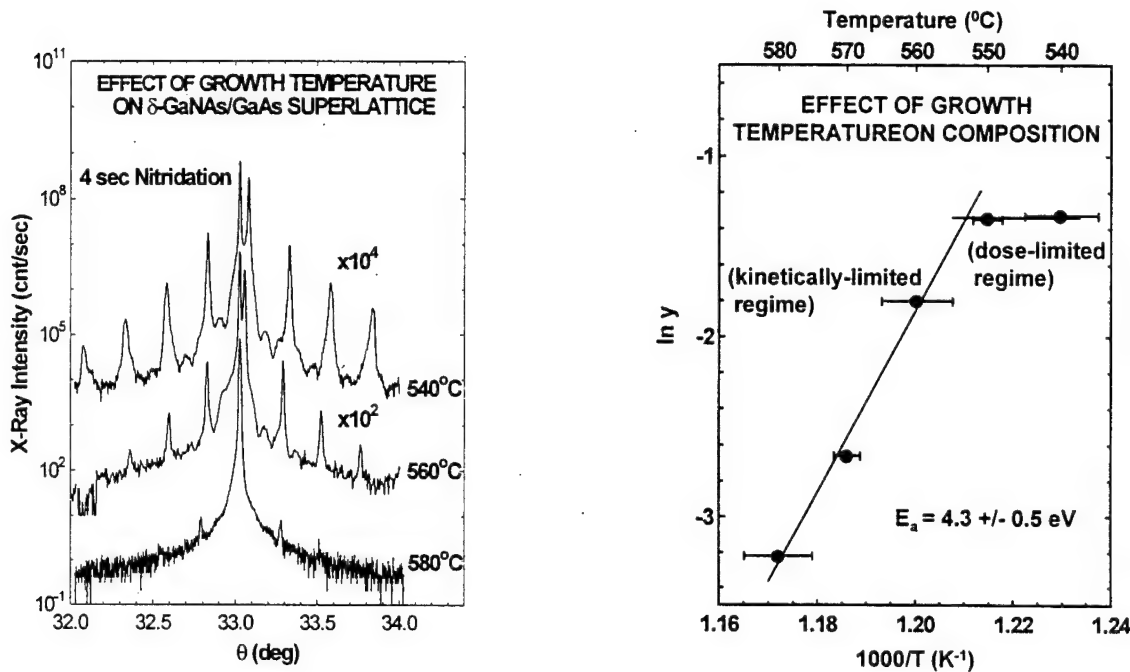


Fig. 16. (a) HRXRD about GaAs (004) for $\text{GaN}_y\text{As}_{1-y}/\text{GaAs}$ superlattice structures. Results indicate a strong dependence of y on growth temperature. (b) Arrhenius plot, showing the effect of growth temperature on y . A thermally activated loss mechanism for the N is suggested. Low-T (dose-limited) and high-T (kinetically-limited) regimes are also seen.

Under this program, we have developed a first-order kinetic model to describe the effects of concurrent the N surface-desorption/surface-segregation processes during MBE growth of our $\text{GaN}_y\text{As}_{1-y}/\text{GaAs}$ superlattices. This modelling effort was performed in collaboration with the group of Prof. T. C. McGill at Caltech. In our kinetic model, the superlattice N content per monolayer y is given by

$$y = F_i \tau (1 - e^{-t_{\text{exp}}/\tau}) \times \left[\frac{\tau_d + \tau_s}{\tau_d + \tau_s e^{-t_{\text{ml}}/\tau}} \right]$$

where F_i is the effective incident N flux, t_{exp} and t_{ml} are the experimental plasma exposure and GaAs monolayer overgrowth times, respectively, and the t terms are kinetic rate constants for the thermally activated processes: t_d (t_s) describes N surface-desorption (surface-segregation) and is of the form, $t_d = t_{d0} \exp(-E_d/kT)$, where E_d is the activation energy for desorption (with a similar relation for t_s), with $t = (1/t_d + F_i)^{-1}$. This model implicitly reflects the specific growth sequence (nitridation, GaAs overgrowth, As soak) of each period of our $\text{GaN}_y\text{As}_{1-y}/\text{GaAs}$ superlattices, and explicitly describes, within the framework of a first-order rate-kinetics theory, the relevant microscopic processes of N surface segregation with simultaneous surface desorption. Applicability of the model to our samples is clear from Fig. 17, which compares the predicted N content from the model (solid curve) with the actual experimentally observed values. Also evident is the importance of including the surface segregation process in the growth model: the dashed curve represents the model prediction in the absence of surface segregation, and clearly, deviates substantially from the experimental values. The detailed agreement

between model and experiment serves to confirm the existence of the assumed microscopic growth processes, and, additionally, permits an assessment of their kinetics: our entire set of substrate-temperature-dependent HRXRD, as well as our earlier RHEED (see previous report) observations, are now consistently explained by our kinetic model assuming N surface-desorption and -segregation processes during nitride/arsenide ECR-MBE growth have activation energy values, $E_d = 2.1 (\pm 0.1)$ eV and $E_s = 0.9 (\pm 30\%)$ eV, respectively.

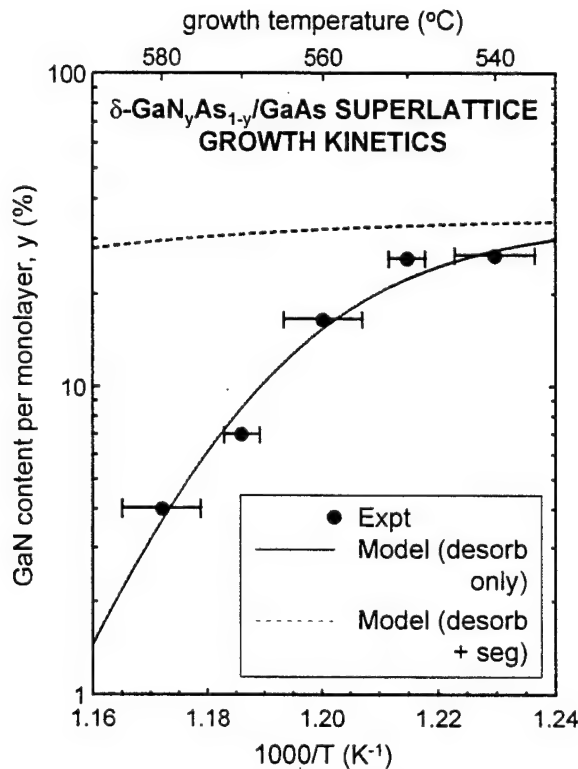


Fig. 17. Growth kinetics models, to explain the strong $y(T)$ dependence observed for ECR-MBE-grown $\text{GaN}_{y}\text{As}_{1-y}/\text{GaAs}$ superlattices.

c. Cross-sectional STM Studies

To further understand the microstructure of our $\text{GaN}_{y}\text{As}_{1-y}/\text{GaAs}$ superlattices, cross-sectional scanning tunneling microscopy (x-STM) studies were performed. These x-STM measurements were performed at IBM Thomas J. Watson Research Center, and, later, at Carnegie-Mellon University, in collaboration with Prof. R. M. Feenstra, and his associate, Dr. Rachel Goldman.. Prof. Feenstra is one of the world's leading STM scientists, and one of the pioneers of STM research in the U.S. For STM studies, the samples were cleaved to expose a (110) surface, in an ultra-high-vacuum chamber with base pressure $< 4 \times 10^{-11}$ Torr. The x-STM was performed with electrochemically etched single-crystal <111>-oriented W tips cleaned by *in situ* electron bombardment and characterized by *in situ* field-emission microscopy. Typically, images were obtained with a constant tunnel current of 0.1 nA. Details of the STM design, cleavage procedure, and spectroscopic methods have been described previously.

Figures 18(a) and 19(a) below show x-STM topographic images of the $\text{GaN}_x\text{As}_{1-x}/\text{GaAs}$ superlattices, displayed with the growth direction going from right to left. In these empty-state images, the nitrided regions appear as depressions (darker regions) in the surrounding GaAs (brighter regions). The large-scale image in Fig. 18(a), acquired at sample bias voltage of +2.2 V, indicates that the nitrided layers are not continuous films, but consist of groups of atomic-scale defects and clusters of various sizes. In Fig. 19(a), we present a high-resolution view of the superlattices, acquired at a sample bias voltage of +2.5 V. Fringes with a spacing of 5.65 Å, corresponding to the (001) lattice planes of GaAs, are observed in the bright regions of the image. The image consists primarily of one nitrided layer sandwiched by 160 Å GaAs layers, with tails of additional nitrided layers on the edges of the image. This nitrided layer contains one small cluster and a group of atomic scale defects. It is evident that the extent of nitrogen incorporation in the growth direction is over 30 Å, considerably greater than the simulated monolayer thickness. In filled state images (negative sample bias voltage), the nitrided regions appear bright in comparison with the surrounding GaAs. Since the contrast of the defects and clusters is dependent on the sign of the bias voltage, both features are of electronic rather than topographic origin. In other words, the dark (bright) features in the empty (filled) state images are not pits (protrusions) in the surface but instead regions with different electronic structure.

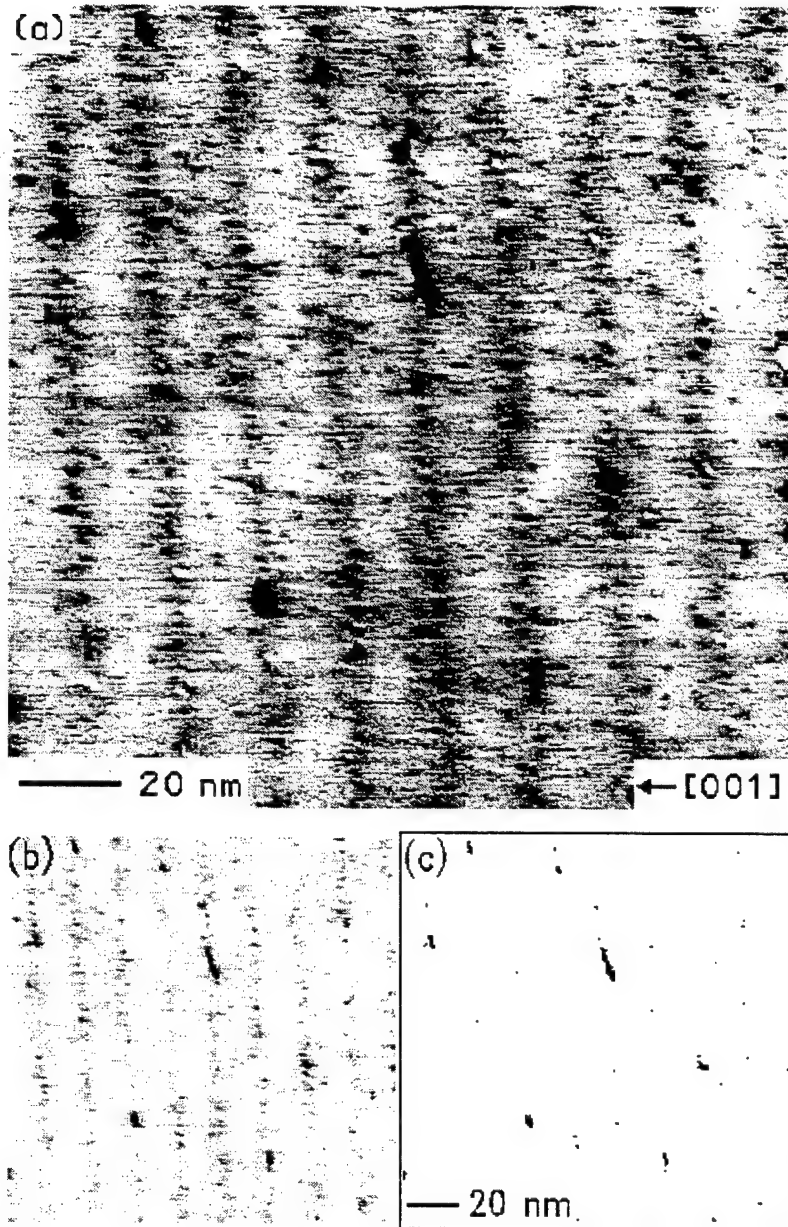


Fig. 18. Large-scale topographic images of GaN/GaAs superlattices, acquired at a sample voltage of +2.2 V. The grey-scale ranges displayed in (a) and (b) are 2.1 and 4.7 Å, respectively. In (c), pixels with tip height more than 2 Å below the nominal GaAs height are displayed as black, while all others are white.

In order to quantify the nitrogen content in the structures, we have determined the fractional area of clusters in several large-scale images such as Fig. 18(a). We used an algorithm to count pixels in regions of the image with tip height below a specified value. We estimate a tip height (depth) criterion based on the tip height profile in the vicinity of a cluster. Figure 19(c) is a line cut of the tip height, taken through the center of a cluster, defined by the arrows in Fig. 19(a). The line cut indicates a region of decreased tip height at the cluster, surrounded by a gradual

increase in tip height, presumably due to band bending at the cluster/GaAs interface. It is evident from this line cut that the band bending is partly superposed on the GaAs atomic corrugation. This effect is further illustrated for the small cluster outlined by a white box in Fig. 19(a). In Fig. 19(b), the grey-scales in the white box region are expanded from 2.7 to 4.7 Å, and the apparent size of the cluster is significantly reduced. Thus, part of the contrast displayed in the clusters in Figs. 18(a) and 19(a) is due to band bending and must be taken into account when counting up the total cluster area. Therefore, the tip height cutoff is defined as the depth at which the atomic corrugation is not observed, approximately 2 Å below the unperturbed GaAs regions. In Figs. 18(b) and (c) we show our analysis of cluster density performed on several large-scale images such as Fig. 18(a). In Fig. 18(b), the grey-scales of Fig. 18(a) are expanded from 2.1 to 4.7 Å. In Fig. 16(c), image pixels with tip height more than 2 Å below the nominal GaAs height are displayed as black, while all other image pixels are white. The fraction of black regions is $4.45 \pm 0.05 \times 10^{-3}$, which corresponds to only ~ 0.2 monolayer of GaN per deposited layer, rather than the full monolayer assumed earlier. A similar fractional area of clusters is obtained in several large-scale images, with total area under 0.2 mm^2 . HRXRD results, similar to those in Fig. 16(a), indicate an average superlattice lattice constant, 5.6499 Å, previously interpreted in terms as continuous monolayers of $\text{GaN}_{0.21}\text{As}_{0.79}$ sandwiched between 192 Å GaAs layers. Now, with the knowledge of the fractional area of the clusters provided by spatially resolved STM imaging, we estimate a cluster lattice constant of 4.6 ± 0.1 Å, similar to bulk GaN. This suggests that the nitrided regions consist of *phase-segregated* GaN embedded within GaAs, rather than some intermediate GaNAs ternary alloy in a continuous layer.

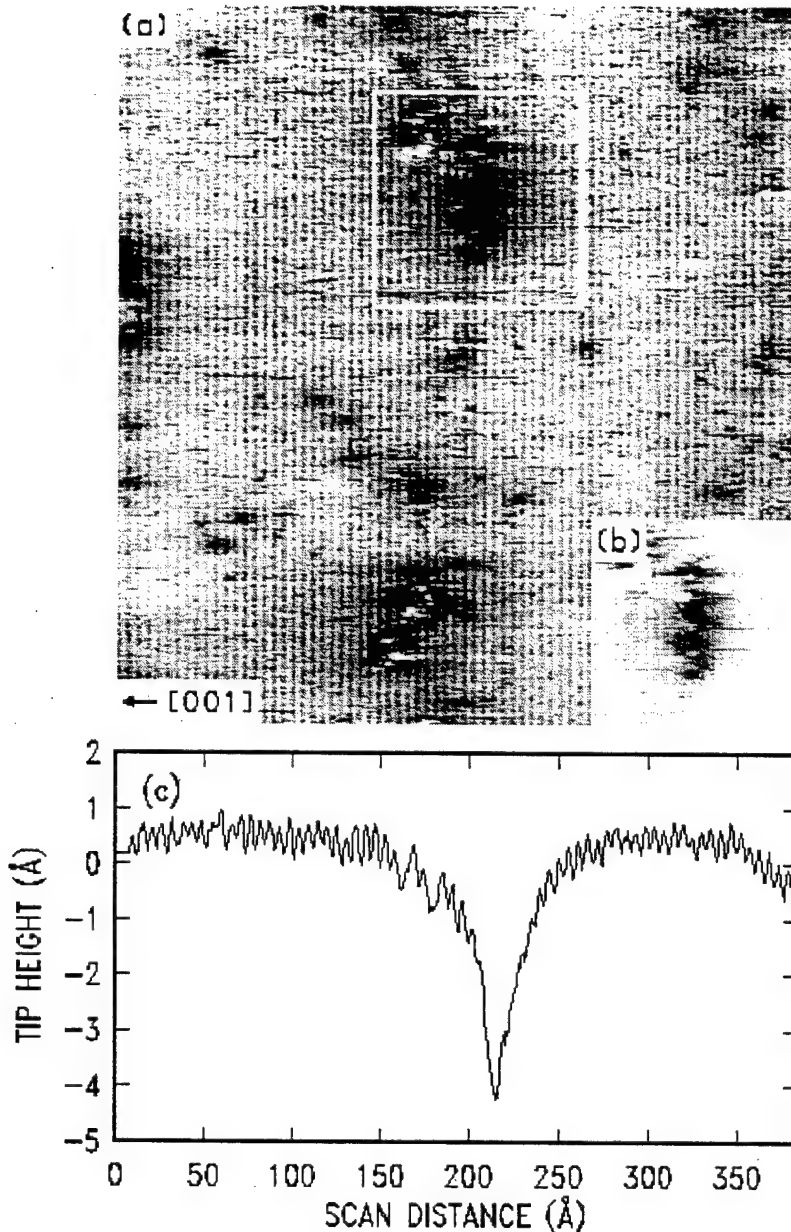


Fig. 19. High resolution topographic image acquired at a sample voltage of +2.5 V. The grey-scale range displayed in (a) is 2.7 Å. A view of the region outlined by a white box in (a) is shown in (b), with a grey-scale range of 4.7 Å. A cut along the line indicated by arrows in (a) is displayed in (c).

In order to chemically identify the atomic-scale defects and clusters, we performed spectroscopic measurements on individual defects and clusters of various sizes. In Figs. 20 (a) and (b), the normalized conductance versus sample bias voltage are plotted for an atomic scale defect (GaAs:N) and large cluster (lateral extent > 50 Å), respectively, and compared with regions of clean GaAs. The GaAs spectra, shown at the bottom of both figures, display well-defined band edges (the band edge positions are determined by assuming a linear onset in the normalized conductance, with a band gap of 1.43 ± 0.10 eV, comparable to that of bulk GaAs. The nonzero

conductance within the GaAs gap in Fig. 20(b) is the "dopant-induced" component, which arises from electrons tunneling out of filled conduction band states. In Fig. 20(a), the spectrum corresponding to atomic scale defects displays well-defined band edges and band gap similar to GaAs. However, in this case, a state is observed at 0.40 ± 0.05 eV above the conduction band edge. The position of this state with respect to the conduction band edge is consistent with predictions for N isoelectronic traps in GaAs. Therefore, we associate the state with an acceptor level of N_{As} in GaAs, and identify the atomic-scale defects as N_{As} .

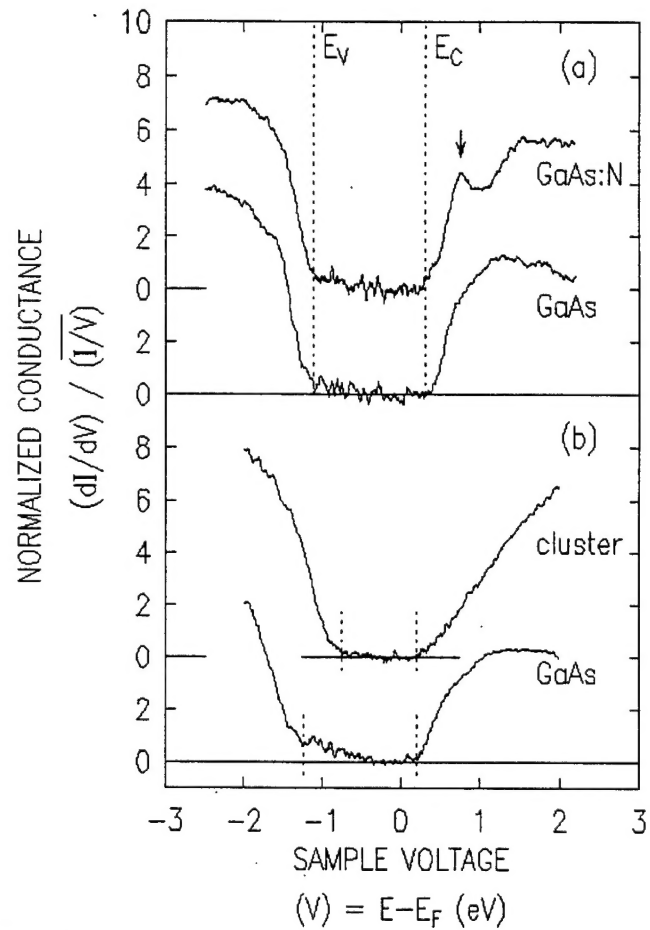


Fig. 20. STM spectra acquired on (a) atomic scale defect (GaAs:N) and (b) large cluster (lateral extent > 50 Å), in comparison with regions of clean GaAs. The valence and conduction band edges are marked by E_V and E_C , respectively. In (a), the state associated with an acceptor level of N_{As} in GaAs is indicated by a downward pointing arrow. The sample voltage corresponds to the energy of the state relative to the Fermi level.

11. High-Precision Lattice Parameter Measurements

A preliminary attempt to make high-precision (to 5 significant figures) absolute lattice parameter measurements of wurtzite GaN films for the purpose of strain assessment has been made through the use of our HRXRD (Philips MRD, 4-bounce monochromator) system. Unlike conventional X-ray rocking curve methods, which typically require measurement merely of the *relative offset* from a substrate peak of known lattice parameter, the present measurements must be made without reference to the substrate, since the substrate itself is strained by the film by an unknown amount which varies from sample to sample. Hence, in this work, the *absolute* Bragg angle must be determined (as precisely and accurately as possible).

Briefly, our method involves careful measurement of essentially two quantities: (i) c lattice parameter, and (ii) c/a ratio. In practice, each of these "single" measurements is in fact a carefully chosen set of measurements, performed in such a way as to minimize both systematic and random measurement errors. In particular, c is obtained from measurements of the (002), (004), and (006) symmetric Bragg reflections, where each of these is in turn measured with the sample aligned along four different azimuths. Next, a plot of $(2 \sin q_n / l)$ vs. n , an integer, where n is the Miller index of the corresponding $(00n)$ reflection, is made in each data point is given a rigorously correct statistical weighting. The accuracy of this approach derives from the lack of error in the abscissa, since, when plotting against integers, the values are quantized. An implicit check on the validity of the data set is the linearity of the plot thus obtained. The slope then directly yields best estimates for both c and its associated uncertainty, following standard linear regression techniques. In an analogous, but somewhat more complex fashion, combinations of several distinct asymmetric measurements [of the form, $(h,0,l)$], were used to determine similarly the c/a ratio and its uncertainty.

We must stress that our results are *preliminary*: our data are of as yet unpublished. We expect to make an upgrade to our HRXRD system during the final year of this program. This upgrade will greatly facilitate the reliability of high-precision, absolute, lattice parameter measurements (and will be based on a direct measurement of the scattering angle $2q$ rather than the "rocking" angle w .) With this caveat, we show our preliminary absolute lattice parameter measurements below in Figure 22. As seen in the figure, a and c lattice parameters have been determined for several wurtzite GaN films grown on sapphire and on SiC substrates. In general, GaN possesses both a lattice-parameter as well as thermal-expansion coefficient mismatch. In principle, both may give rise to residual stress in the epitaxial film, though, in practice, for films greatly in excess of their critical thickness for coherently strained epitaxy, the films should be largely relaxed at the epitaxial growth temperature, and, hence, should encounter stress due to differing rates of thermal contraction as the epi/substrate combination is cooled, but not allowed to relax plastically on the interfacial plane. In this situation, the observed residual strain in

room-temperature GaN films should be predominantly that due to this differential-thermal-contraction stress, rather than to lattice-constant mismatch. This is indeed strongly suggested by our work: all films grown on C-sapphire are under biaxial *compression* while those on SiC are under biaxial *tension*. This is consistent with the *opposite algebraic signs* of differential thermal mismatch, but inconsistent with the *like algebraic signs* of lattice constant mismatch, based on the widely accepted material values for GaN, sapphire, and SiC. Finally, of particular interest in lattice mismatched epitaxy is the biaxial strain ratio (ratio of c-strain to a-strain). This is calculable from the elastic constants (ratio = $2c_{33}/c_{11}$ in this case), but, unfortunately, due to the unavailability of high quality bulk GaN materials, accurate values are not available. Thus, even our *preliminary* estimate of the biaxial strain ratio, ~0.5 is a significant numerical result.

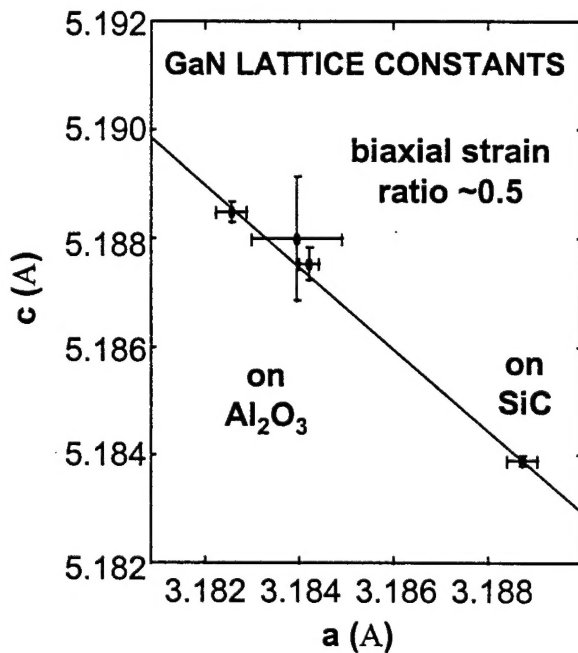


Fig. 22. Preliminary measurement of lattice parameters for strained, wurtzite GaN films on the most widely used substrates. Due to differential thermal contraction of the film/substrate combination upon cooling from the epitaxial growth temperature, a biaxial stress is applied to the film (and substrate) in the interfacial plane. Films on C-sapphire are under biaxial compression; films on SiC are under tension.

12. COMPARISON OF ECR AND RF PLASMA SOURCES

Recently, under a related research program, we have obtained and installed an RF plasma source on our ECR-MBE growth system. To date, most of our RF-MBE GaN growth has concentrated on growth of wurtzite GaN layers on sapphire substrates. However, we have, as of this writing, made a very preliminary but interesting observation regarding the comparison of the ECR and RF- plasma sources for nitride growth. In our 1-July-1994 progress report for this AASERT

program, we reported the growth of our first GaN films (on GaAs). These films were *zinc blende*. Recently, when we attempted to reproduce these earlier results in testing our new RF source (SVT Associates), we observed that the films, under otherwise comparable MBE growth conditions, were *wurtzite* predominantly. Upon inspection of the literature, we have noted that, for given growth conditions of GaN on (100) GaAs, a wide range of crystallographic structure and quality, from purely *zinc blende*, to mixed, to purely *wurtzite*, have been reported. The significant difference appears to be the type of plasma source used: ECR sources (both Wavemat and Astex) seem to produce the metastable *zinc blende* phase directly, whereas RF sources (Oxford, SVT Associates) yield the thermodynamically preferred *wurtzite* form unless kinetic barriers to growth are deliberately introduced. Thus, the important observation appears to be that the available RF plasma sources in general are more amenable to the growth of the thermodynamically preferred phase of GaN. It is also known that higher growth rates (without the sacrifice of material quality) is obtainable from RF in comparison with ECR sources. This is possibly explained by the higher fraction of monomeric (as opposed to dimeric) nitrogen radicals in the RF plasma, where more reactive atomic radicals might be expected to more readily surmount reaction kinetic barriers to reach the thermodynamically most favored (*wurtzite*) form of the film. Ion content may also be lower. In any event, RF and ECR plasmas, as produced by commercially available sources for MBE growth, appear to differ substantially (perhaps analogously to the use of cracked vs. uncracked As for GaAs MBE growth) in their ability to controllably nucleate a particular mode of growth under a given set of ambient conditions.